Geochemistry Geophysics Geosystems G3

*Article*
Volume 14, Number 4
5 April 2013
doi:10.1002/ggge.20075
ISSN: 1525-2027

Published by AGU and the Geochemical Society

# Velocity-conductivity relations for cratonic lithosphere and their application: Example of Southern Africa

**Alan G. Jones and Mark R. Muller**
*Dublin Institute for Advanced Studies, 5 Merrion Square, Dublin 2, Ireland (alan@cp.dias.ie)*

**Stewart Fishwick**
*Department of Geology, University of Leicester, Leicester, UK*

**Rob L. Evans**
*Department of Geology and Geophysics, Woods Hole Oceanographic Institution, Woods Hole, Massachusetts, USA*

**Javier Fullea**
*Dublin Institute for Advanced Studies, Dublin, Ireland*

*Institute of Geosciences, CSIC-UCM, Madrid, Spain*

[1] Seismic velocity is a function of bulk vibrational properties of the media, whereas electrical resistivity is most often a function of transport properties of an interconnected minor phase. In the absence of a minor conducting phase then the two should be inter-relatable primarily due to their sensitivity to temperature variation. We develop expressions between shear wave velocity and resistivity for varying temperature, composition, and water content based on knowledge from two kimberlite fields: Jagersfontein (Kaapvaal Craton) and Gibeon (Rehoboth Terrane). We test the expressions through comparison between a new high-resolution regional seismic model, derived from surface wave inversion of earthquake data from Africa and the surrounding regions, and a new electrical image from magnetotelluric (MT) data recorded in SAMTEX (Southern African Magnetotelluric Experiment). The data-defined robust linear regression between the two is found to be statistically identical to the laboratory-defined expression for 40 wt ppm water in olivine. Cluster analysis defines five clusters that are all geographically distinct and tectonically relate to (i) fast, cold, and variably wet Kaapvaal Craton, (ii) fast and wet central Botswana, (iii) slow, warm, and wet Rehoboth Terrane, (iv) moderately fast, cold, and very dry southernmost Angola Craton, and (v) slow, warm, and somewhat dry Damara Belt. From the linear regression expression and the MT image we obtain predicted seismic velocity at 100 km and compare it with that from seismic observations. The differences between the two demonstrate that the linear relationship between $V_s$ and resistivity is appropriate for over 80% of Southern Africa. Finally, using the regressions for varying water content, we infer water content in olivine across Southern Africa.

**Components:** 12,600 words, 18 figures, 6 tables.

**Keywords:** continental lithosphere; cratons; velocity; resistivity.

**Index Terms:** 7218 Seismology: Lithosphere (1236); 1515 Geomagnetism and Paleomagnetism: Geomagnetic induction; 3909 Mineral Physics: Elasticity and anelasticity.

**Received** 25 September 2012; **Revised** 23 January 2013; **Accepted** 23 January 2013; **Published** 5 April 2013.

Jones A. G., S. Fishwick, R. L. Evans, M. R. Muller, and J. Fullea (2013), Velocity-conductivity relations for cratonic lithosphere and their application: Example of Southern Africa, *Geochem. Geophys. Geosyst.*, *14*, 806–827, doi:10.1002/ggge.20075.

## 1. Introduction

[2] Seismic and electromagnetic methods offer complementary information about the subsurface of the Earth. Whereas seismic methods are predominantly sensitive to vertical and lateral variations in bulk properties that are mechanical vibrational parameters, low frequency electromagnetic methods are sensitive to variations in electrical conductivity, which is essentially a transport parameter. Often electrical conductivity is a function of minor, well-interconnected conducting constituents in the rock matrix that can considerably enhance electrical conductivity through electronic or ionic conduction [e.g., *Duba and Shankland*, 1982; *Jones*, 1992; *Roberts and Tyburczy*, 1999; *Yoshino*, 2010; *Jones et al.*, 2012]. As such, taken together the two provide powerful complementary insights into structures and geometries within the Earth [e.g., *Jones*, 1998; 1999], from which inferences can be made about formation and deformation processes [e.g., *Davis et al.*, 2003].

[3] However, for regions of the Earth where contributions from minor conductive (exotic) phases are either absent or are effectively absent through lack of interconnection, for example within dry cratonic lithosphere or "wet" lithosphere that can be characterized by its known water content, conductivity and seismic velocity are both bulk measures of physical state within the Earth (temperature, pressure, bulk composition), and a correlation between seismic parameters and electrical parameters is to be expected. Using a petrological approach based on laboratory observations of individual minerals dominant in cratonic lithosphere (olivine, pyroxenes, and garnet) coupled with an appropriate mixing law, it is possible to define parametric relationships between velocity and conductivity for given temperature, pressure, composition (modal mineral percentages and individual mineral magnesium numbers), and water contents [*Jones et al.*, 2009a; *Fullea et al.*, 2011; *Jones et al.*, 2012].

[4] In this paper, we use that approach to predict the relationship that should exist between shear wave velocity and electrical resistivity at a depth of 100 km beneath southern Africa and test whether the prediction matches the reality of the observed high spatial qualitative correlation between the two geophysical parameters derived from surface wave modeling [*Fishwick*, 2010] and magnetotelluric (MT) data depth imaging [*Jones et al.*, 2009b], as shown in *Jones et al.* [2009b]. We demonstrate that a linear relationship between 1/log(resistivity) and shear wave velocity, as suggested by equations of state assumed when fitting laboratory measurements, is upheld, which explains 80% of the data to within error. That means we can predict seismic velocity from resistivity for over 80% of southern Africa, 95% of cratonic regions, and vice versa, i.e., we can predict resistivity from velocity, with an expression that is consistent with the laboratory observations for an average bulk water content of 40 wt ppm in olivine, 200 ppm in orthopyroxene, 300 ppm in clinopyroxene, and 0 ppm in garnet.

[5] Cluster analysis of the cross-plot between 1/log (resistivity) and shear wave velocity identifies five clusters of points that, when projected onto the map of Southern Africa, are shown to be tectonically correlated. Each of the groups has a distinct velocity and resistivity pairing, and the centroids of the groups yield average temperatures and water contents for that cluster.

[6] Reasons for departure from the laboratory-based predictions must be due to effects on conductivity that increase it by one or more orders of magnitude but that have little concomitant effect on elastic moduli or density so seismic velocity is virtually unaffected. This is true for the region that experienced Bushveld magmatism and also for the younger mobile belts, particularly the Namaqua-Natal, where the lithosphere is thinned and close to our depth of investigation of 100 km.

## 2. Inferences on the Correlation between Seismic Velocity and Electrical Conductivity from Laboratory Measurements

[7] Laboratory measurements of the elastic moduli and electrical conductivity of the four dominant mantle minerals in cratonic lithosphere, namely, olivine (Ol), two pyroxenes (orthopyroxene, Opx, and clinopyroxene, Cpx), and garnet (Gt), obtained from mantle xenoliths yield a range of parametric descriptions. These are compared and contrasted

in *James et al*. [2004] and *Kuskov and Kronrod* [2006] for moduli and density, in *Jones et al*. [2009a] for moduli, density, and electrical conductivity, and recently in *Fullea et al*. [2011] for electrical conductivity, who included the effects of water content. *Jones et al*. [2012] considered the electrical conductivity water models recently derived by the three laboratories making the appropriate difficult laboratory measurements, namely, those of S.-I. Karato [*Wang et al*., 2006b], T. Yoshino [*Yoshino et al*., 2009], and B. Poe [*Poe et al*., 2010], and demonstrated that none of the three models fit the geophysical-petrological data for two regions of Southern Africa. Accordingly, *Jones et al*. [2012] determined their own model for proton conduction due to hydrogen diffusion, which is the one adopted here. The parameters and equations modified from *Fullea et al*. [2011], with modifications discussed in *Jones et al*. [2012], are used here for dry assemblages when small polaron conduction dominates.

## 2.1. Parameters for Bulk and Shear Moduli

[8] The parameters for the bulk and shear moduli and density at pressure and temperature ($P$, $T$) based on their values at room temperature and pressure and derivatives with respect to temperature and pressure are given by

$$\begin{aligned} (K_S)_{P,T} &= K_S + (\partial K_S/\partial P)\Delta P + (\partial K_S/\partial T)\Delta T\ , \\ G_{P,T} &= G + (\partial G/\partial P)\Delta P + (\partial G/\partial T)\Delta T\ , \\ \rho_{P,T} &= \rho(1 - \alpha\Delta T + \Delta P/K_T), \text{ where} \\ K_T &= (K_S)_{P,T}/(1+\alpha\gamma T), \end{aligned} \quad (1)$$

[9] where $K_S$ is the adiabatic bulk modulus, $K_T$ is the isothermal bulk modulus, $G$ is the shear modulus, $\Delta T$ is the temperature difference to 20°C, $\Delta P$ is the pressure difference to 1 bar, $\alpha$ is the thermal expansivity, $\gamma$ is the Grüneisen parameter, and $T$ is temperature in Kelvin. The parameters for individual minerals are listed in Table 1 and are primarily based on *James et al*. [2004], with updates from D. James (pers. comm., 2011), and with additional terms for iron content in Cpx from *Goes et al*. [2000] and for the density of garnet from *Liu and Li* [2006]. The parameters in Table 1 are optimized for magnesium numbers (Mg#) within each mineral of around 90–91, representative of depleted upper mantle peridotite.

## 2.2. Parameters for Electrical Conductivity

[10] Conduction in a mantle mineral is given by the sum of three effects, namely,

**Table 1.** Bulk and Shear Moduli for the Five Minerals and Their Variation with $T$ and $P$, and the Density, Thermal Expansivity, and Gruneisen Parameter[a]

| | $K_S$ (GPa) | δK/δP | δK/δT | G (GPa) | δG/δP | δG/δT | ρ(g/cc) | α($10^{-4}$) | γ |
|---|---|---|---|---|---|---|---|---|---|
| Ol | 128.6 +7.0*f* | 4.40−2.0*f* | −0.0182−0.00009*f* | 79.1 −35.8*f* | 1.71 −1.23*f* | **−0.0124** | −0.00018*f* | 3.22 +1.32*f* | 0.285 −0.047*f* | 1.15 +0.6*f* |
| Opx | 106.5 −5.2*f* | **10.0** −2.56*f* | −0.0268 | 75.0 | 1.60 | | **−0.0119** | 3.21 +0.80*f* | 0.270 +0.037*f* | 0.875 |
| Cpx | 113.0 ***+13f*** | 4.8 | −0.0149 | 67 ***−6.0f*** | 1.7 | | −0.010 | 3.277 +0.38*f* | 0.232 | 1.50 |
| Gt | **172.0** | 4.9 | −0.0195 | 93.0 | 1.56 | | −0.010 | ***3.565 +0.76f*** | 0.236 | 1.30 |
| Sp | 198.0 | 5.5 | −0.0291 | 108.5 | 0.072 | | **0.0121** | 3.58 | 0.249 | 1.17 |

[a] α is thermal expansivity, γ is Gruneisen parameter, *f* is iron number, given by 1.-(Mg#/100). Values taken from *James et al*. [2004] except where noted. **Bold** values are updates provided by D. James [pers. comm., 2011]. ***Bold italic*** values for iron content of Cpx from *Goes et al*. [2000], and for density of Gt from *Liu and Li* [2006].

$$\sigma = \sigma_0 \exp\left(\frac{-\Delta H(X_{Fe}, P)}{kT}\right) + \sigma_{0i} \exp\left(\frac{-\Delta H_i}{kT}\right) + f(C_w) \exp\left(\frac{-\Delta H_{wet}(C_W)}{kT}\right),$$

where

$$\Delta H(X_{Fe}, P) = a + bX_{Fe} + cX_{Fe}^2 + dX_{Fe}^3 + cX_{Fe}^4 + fX_{Fe}^5 + P\Delta V, \quad (2)$$

[11] [*Fullea et al.*, 2011], where the first term describes small polaron conduction, the second term describes Mg vacancies conduction, and the third term describes proton conduction by hydrogen diffusion in the water-present case.

[12] For electrical conductivity, the equations of state for mantle minerals are reviewed in detail in *Jones et al*. [2009a], *Fullea et al*. [2011], and *Jones et al*. [2012], to which the reader is referred. As shown in *Jones et al*. [2012], proton conduction through the diffusion of hydrogen dominates over small polaron conduction even for very low amounts of water (10 wt ppm). Conduction by magnesium vacancies is unimportant at the temperatures considered here. For completeness though, our calculations are undertaken with all three processes considered, and the aggregate conductivity is given by the sum of the three parallel effects. All parameters used for electrical conductivity are listed in Table 2.

[13] One important point to note here, as will be demonstrated later, is that conductivity has far higher sensitivity to temperature variation than does velocity. This can be seen by comparing equation (1) with (2); conductivity varies exponentially with inverse temperature (equation (2)), whereas the seismic moduli vary linearly with temperature (equation (1)), thus velocity varies linearly, to first order in a Taylor series expansion, with temperature.

## 2.3. Focus at Depth of 100 km

[14] We focus on results at a depth of 100 km for our correlation study. The choice of this depth is made for three main reasons.

1. Firstly, at 100 km the resolution of the surface wave study should provide reliable estimates of the uppermost mantle velocities. At shallower depths, there is the potential for mixing of crustal and mantle velocities. At depths greater than 100 km, resolution decreases as the dominant information is from the longer period surface waves that have broad sensitivity kernels, and there will thus be mixing of upper lithospheric

**Table 2.** Parameters for Conductivity Equations of *Fullea et al.* [2011] with the Water Model Taken from *Jones et al.* [2012][a]

| | Small Polaron Conduction | | | | | | | | Mg Vacancies Conduction | | Proton Conduction | | | |
|---|---|---|---|---|---|---|---|---|---|---|---|---|---|---|
| | Log $\sigma_0$ | $a$ | $b$ | $c$ | $d$ | $e$ | $f$ | $\Delta V$ | log $\sigma_{0i}$ | $\Delta H_i$ | log $\sigma_0$ | $r$ | $\Delta H_{wet}$ (eV) | $\alpha$ |
| Ol | 2.4–3.0 | 1.642 | 0.246 | −4.85 | 3.259 | - | - | 0.68 | 4.73 | 2.31 | 3.05 ± 0.16 | 0.86 ± 0.08 | 0.91 ± 0.03 | 0.09 ± 0.08 |
| Opx | 2.4–3.72 | 1.9 | −2.77 | 2.61 | −1.09 | - | - | - | - | - | 2.6 | 0.62 | 0.85 | *1.1* |
| Cpx | 3.25 | 2.075 | −2.77 | *2.61* | *−1.09* | - | - | - | - | - | *2.6* | *0.62* | *0.85* | *1.1* |
| Gt | (2.67–3.39) + log(1 − 0.044P) | 2.6 | −15.33 | 80.4 | −194.6 | 202.6 | −75 | 2.5 | 4.96 | 2.05 | 2.29 | 0.63 | 0.725 | *1.1* |

[a]Those in italics are assumed as no measurements exist.

and lower lithospheric, and even asthenospheric, velocities, especially in regions of thinned lithosphere. At mantle depths of 100 km, using the two-stage multimode inversion technique [*Fishwick*, 2010], the approximate vertical resolution is around ±25 km.

2. Secondly, for MT studies, conducting material in the crust will result in a "shadow zone" in the uppermost mantle directly beneath the Moho within which one can only define its minimum resistivity value, not its actual value [*Jones*, 1999]. By 100 km, however, the effects of the crustal attenuation are reduced, and the resistivity can typically be resolved (see Figure 3 in *Jones* [1999]). In Southern Africa, crustal conductivity is nowhere as high as that in Figure 3 of *Jones* [1999], so superior resolution is expected of mantle resistivity than depicted in that figure. Nevertheless, to avoid potentially biased results from the uppermost lithosphere, 100 km is chosen.
3. Finally, we choose 100 km to avoid problems associated with anelastic behavior of mantle minerals as they approach adiabatic temperatures at the base of the lithosphere, as our characterization of the rock assemblages is based purely on anharmonic derivatives. For cratonic regions, we could go down to depths of 150–200 km, but off-craton areas, where the lithosphere-asthenosphere boundary is relatively shallow (150 km or so from geophysical and petrological studies), we anticipate errors even at 125 km depth.

## 2.4. Xenolith Information

[15] For petrological characterization of the lithosphere at 100 km, we take as representative end-members xenolith information from two kimberlite fields, (1) the Jagersfontein field in the eastern Witwatersrand Block of the Kaapvaal Craton and (2) the Gibeon field in central Namibia on the Rehoboth Terrane, the former being depleted and the latter fertile. The xenoliths are discussed in detail in *Jones et al*. [2012]; we pick two representative low-temperature, garnet lherzolite xenoliths from each kimberlite field that yield depths close to 100 km. Their modal compositions are listed in Table 3, as well as their in situ temperature estimates. Group I kimberlites of the Kaapvaal Craton and neighboring mobile belts erupted in the period 105–70 Ma [*Kobussen et al*., 2009]. Subsequent thermal relaxation since eruption will result in colder conditions than those indicated by the xenolith samples, and thermal arguments suggest a present-day temperature of around 740°C beneath the Witwatersrand Basin in the center of the Kaapvaal Craton [*Jones*, 1988]. The present-day geotherm beneath the Rehoboth Terrane is known to be higher than beneath the Kaapvaal Craton [*Muller et al*., 2009], consistent with the conditions at kimberlite eruption. Therefore, we adjust the xenolith-determined temperatures downwards by 50°C to give estimates of present-day temperatures of 740°C and 850°C at 100 km beneath Jagersfontein and Gibeon, respectively. A temperature decrease of 50°C, keeping all other petroparameters constant, increases velocity by 0.02–0.03 km/s and reduces conductivity by 0.3–0.4 log units for dry conditions and 0.2 log units for wet conditions (see below for discussion and definition of wet conditions).

## 2.5. Water Content in Cratonic Mantle Minerals

[16] The water content in cratonic nominally anhydrous minerals is becoming better known and understood since the pioneering laboratory experiments by *Bai and Kohlstedt* [1992]. It is now thought that the mantle could host as much as one to five times the water content of the hydrosphere [*Bell and Rossman*, 1992; *Ingrin and Skogby*, 2000] and has played, and continues to play, a governing role in Earth's tectonic processes [*Hirschmann and Kohlstedt*, 2012].

[17] The most comprehensive recent compilation of the water content in olivine for the Kaapvaal Craton is that of *Peslier et al*. [2010], reproduced in Figure 1, who present water contents in the range 40–85 ppm

**Table 3.** Mg#, Modal Composition, and Petrologically Determined Pressures and Temperatures (at Eruption Age) of Four Xenoliths from the Jagersfontein (FRB samples) and Gibeon (KGG samples) Kimberlite Fields (Taken from *James et al*. [2004]), Plus Locality Averages (in bold)

| Sample | Mg# (Ol, Opx, Cpx) | Ol (%) | Opx (%) | Cpx (%) | Gt (%) | Sp (%) | *P* (kbar) | *T* (°C) | *D* (km) |
|---|---|---|---|---|---|---|---|---|---|
| FRB983 | 93.2 | 68.72 | 24.50 | 4.24 | 0.91 | 0.32 | 30.5 | 760 | 98 |
| FRB1007 | 93.2 | 70.28 | 23.84 | 2.56 | 1.79 | 0.32 | 33.1 | 804 | 106 |
| **FRB AV** | **93.2** | **69.50** | **24.17** | **3.40** | **1.35** | **0.32** | **31.8** | **782** | **102** |
| KGG06 | 91.19 | 73 | 11 | 9 | 8 | 0 | 33.2 | 926 | 108 |
| KGG65 | 92.30 | 76 | 12 | 4 | 7 | 0 | 33.5 | 872 | 109 |
| **KGG AV** | **91.75** | **74.5** | **11.5** | **6.5** | **7.5** | **0** | **33.35** | **899** | **108.5** |

(Bell calibration) for various locations on the Kaapvaal Craton at depths of the order of 100 km, based on their own work plus the prior work of *Kurosawa et al*. [1997] and *Grant et al*. [2007]. Added to Figure 1 (solid squares) are the recently published data of *Baptiste et al*. [2012], exhibiting water contents of up to 154 ppm for a sample from Kimberley and the olivine megacryst data from kimberlitic magmas (see *Baptiste et al*. [2012] for further details and references). Given the data of Figure 1, it is reasonable to assume water content in olivine of the order of 50–200 wt ppm at around 100 km depth beneath Jagersfontein. Although not relevant for this paper, note the remarkable very strong decrease in water content in olivine with increasing pressure (depth), such that the lowermost lithospheric mantle comprises essentially dry olivine, consistent with models in which the longevity of cratonic lithosphere is achieved through a high viscosity resulting from a dry composition [*Peslier et al*., 2010].

[18] For the pyroxenes, the averages for South African cratonic samples are $244 \pm 107$ ppm and $397 \pm 61$ ppm for orthopyroxene (Opx) and clinopyroxene (Cpx), respectively, as given in *Xia et al*. [2010]. Global cratonic averages are 157 ppm in Opx and 276 ppm in Cpx [*Peslier*, 2010]. Thus, we assume a constant value of 200 ppm for Opx and 300 ppm for Cpx, regardless of the water content in olivine.

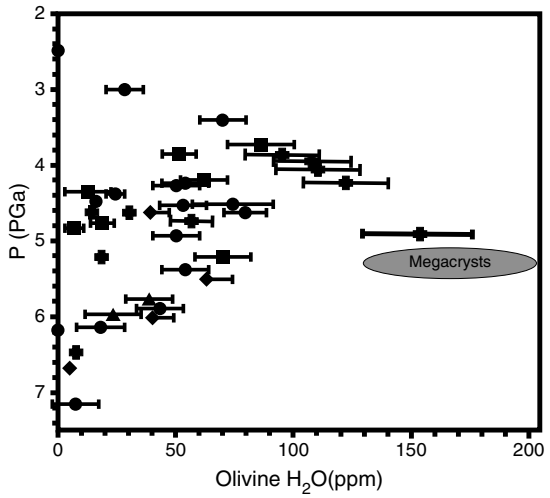


**Figure 1.** Water contents in olivine from various xenolith localities on the Kaapvaal Craton; circles: Lesotho; diamonds: Jagersfontein; triangles: Kimberley; diamonds: Finsch. Reproduced from *Peslier et al*. [2010]. Added to the figure are the data from *Baptiste et al*. [2012] from Kimberley, Jagersfontein, Finch, Premier, and Mothae (solid plus signs), plus the olivine megacrysts in kimberlitic magmas [see *Baptiste et al*., 2012, for detailed information].

This assumption makes little difference, as olivine dominates the modal composition (Table 3).

[19] Garnet displays almost no water whatsoever in xenolith samples, so proton conduction in garnet in the lithosphere can be ignored, and only small polaron conduction in garnet is important. Given the low quantities of garnet in the whole rocks, this decision also hardly affects the calculations.

[20] For the Gibeon kimberlite field on the edge of the Rehoboth Terrane, for which there are no water content data published, we assume the same values as for Jagersfontein. However, as we will derive below, the Rehoboth Terrane is slightly wetter than Jagersfontein—of the order of 100 wt ppm on average rather than 80 wt ppm water in olivine.

## 2.6. Predictions of Conductivity and Velocity Based on Laboratory Studies

[21] We form averages of physical properties for each locality from the two individual samples (Table 3). Following *Jones et al*. [2009a], for the four samples and two averages, we calculate whole rock moduli, density, and conductivity using the ($P$, $T$) conditions and modal compositions from Table 3 and water contents from Table 4, and the formulae in equations (1) and (2) with moduli parameters listed in Table 1. We aggregate the individual minerals using second-order, multiphase Hashin-Shtrikman extremal bounds [*Berryman*, 1995], taking into account possible interfacial processes [*Salje*, 2007].

[22] Using second-order Hashin-Shtrikman bounds for determining the seismic properties of the aggregate material was advocated by *Watt et al*. [1976], who stated "The widely used Voigt-Reuss-Hill average can be a poor approximation for both two-phase composites and polycrystals, and its replacement by the two Hashin-Shtrikman bounds is recommended." Despite this recommendation, use of Hashin-Shtrikman bounds in seismology is rare (see discussion in *Jones et al*. [2009a]). However, for the mineral assemblages considered herein, olivine (Ol) and orthopyroxene (Opx) make up the bulk of the whole rock, over 90% in most cases, and, as the seismic parameters for Ol and Opx are close to one another, all reasonable

**Table 4.** Assumed Water Contents at 100 km below Jagersfontein and Gibeon

| | Ol (%) | Opx (%) | Cpx (%) | Gt (%) |
|---|---|---|---|---|
| Jagersfontein | 80 | 200 | 300 | 0 |
| Gibeon | 80 | 200 | 300 | 0 |

aggregating methods give similar results to one another, as noted previously by *James et al.* [2004]. For electrical conductivity, extremal bounds are more important, as the influence of the highest conductivity phase, even if only a very minor component (1%), can be dramatic if the phase is well connected. In our case however, the four minerals have conductivities that are within an order of magnitude of each other at any given ($P$, $T$) conditions, and again Ol and Opx dominate, so the bounds are not wide. In addition, minerals in xenoliths are characterized by their random geometry rather than ordered, so the geometric mean of the extremal bounds is a reasonable estimator of the bulk resistivity of the composite.

[23] From the moduli and density, we derive bulk, compressional, and shear wave velocities, but herein we are only considering shear wave velocity. The estimates are listed in Tables 5 (velocity) and 6 (conductivity) (note: $\log_{10}$(resistivity) is given in Table 6 rather than $\log_{10}$(conductivity) as we will be comparing these results with observations that are always in terms of resistivity. As resistivity is the reciprocal of conductivity, their logarithms are simply the negative of each other), and summarized in Table 8. Also listed in Table 5 are bulk rock estimates determined from the more commonly used methods in seismology for aggregating minerals, namely, *Voigt* [1928] and *Reuss* [1929] estimates and their arithmetic [*Hill*, 1952] and geometric [*Ji et al.*, 2004] averages, plus the weighted slowness average employed by *James et al.* [2004]. The Voigt and Reuss averages of the moduli represent first-order bounds given by serial and parallel averages of the properties; such averaging procedures are also used in conductivity studies [*Fullea et al.*, 2011].

**Table 6.** Hashin-Shtrikman Estimates of $\log_{10}$(Resistivity [Ωm]) at 100 km Depth beneath Jagersfontein (FRB Samples) and Gibeon (KGG Samples), Assuming Dry Conditions (No Water). Locality Averages in Bold

| Sample | $T$ (°C) | $HS^-$ (S=0) | $HS^+$ (S=0) | $HS^-$ (S=1) | $HS^+$ (S=1) | HS GAV |
|---|---|---|---|---|---|---|
| FRB983 | 710 | 5.53 | 5.20 | 5.49 | 5.49 | 5.43 |
| FRB1007 | 755 | 5.18 | 4.76 | 5.19 | 5.16 | 5.07 |
| **FRB AV** | 740 | 5.30 | 4.96 | 5.29 | 5.28 | **5.21** |
| KGG06 | 875 | 4.34 | 3.86 | 4.36 | 4.24 | 4.20 |
| KGG65 | 825 | 4.68 | 4.12 | 4.71 | 4.59 | 4.52 |
| **KGG AV** | 850 | 4.51 | 3.99 | 4.53 | 4.41 | **4.36** |

[24] The average petrologically based estimates for the velocity and $\log_{10}$(resistivity) at 100 km depth beneath Jagersfontein and Gibeon are [4.67 km/s, 5.21 log units] and [4.61, 4.36], respectively, for dry (water absent) conditions. The different physical conditions (temperature, composition) beneath Jagersfontein and Gibeon therefore produce a difference in velocity of 0.063 km/s (1.35%) and $\log_{10}$(resistivity) of 0.91 (resistivity is reduced by a factor of 8). To test sensitivity to the three parameters [$T$, mineral Mg# (Gt fixed at 75.0) and modal% (Ol, Opx, Cpx, Gt)], we vary each of them linearly from the Jagersfontein parameters [740°C, (Mg# = 3 × 93.2, 75.0), (modal% = 69.50, 24.17, 3.40, 1.35)] to the Gibeon parameters [850, (3 × 91.75, 75.0), (74.5, 11.5, 6.5, 7.5)] individually, and the variations are shown in Figure 2a (for $V_s$) and Figure 2b (for log (resistivity)). Note the linear variation of $V_s$ with varying all parameters and log(resistivity) for composition and Mg# but the exponential variation of log($\rho$) when temperature is varied linearly (cf. equations (1) and (2)). Figure 2b compares the resistivity estimates from the polaron conductivity models of *Jones et al.* [2009a] with those of *Fullea et al.*

**Table 5.** Estimates of Density and Shear Wave Velocity at 100 km Depth beneath Jagersfontein (FRB Samples) and Gibeon (KGG Samples) Using Different Aggregating Methods[a]. Locality Averages in Bold

| Sample | $T$ (°C) | $\rho$ (g/cc) | Voigt | Reuss | Hill | Ji | $Vs$ Average | HS ($S$=0) | HS ($S$=1) | HS GAV |
|---|---|---|---|---|---|---|---|---|---|---|
| FRB983 | 710 | 3.323 | 4.675 | 4.672 | 4.673 | 4.673 | 4.673 | 4.673<br>4.673 | 4.683<br>4.683 | 4.678 |
| FRB1007 | 755 | 3.333 | 4.680 | 4.676 | 4.678 | 4.678 | 4.678 | 4.678<br>4.678 | 4.674<br>4.674 | 4.676 |
| **FRB AV** | 740 | 3.326 | 4.673 | 4.669 | 4.671 | 4.671 | 4.671 | 4.671<br>4.671 | 4.677<br>4.677 | **4.674** |
| KGG06 | 875 | 3.374 | 4.603 | 4.590 | 4.596 | 4.596 | 4.596 | 4.596<br>4.597 | 4.579<br>4.579 | 4.587 |
| KGG65 | 825 | 3.362 | 4.651 | 4.641 | 4.646 | 4.646 | 4.644 | 4.645<br>4.646 | 4.626<br>4.626 | 4.636 |
| **KGG AV** | 850 | 3.368 | 4.625 | 4.614 | 4.620 | 4.620 | 4.620 | 4.619<br>4.620 | 4.601<br>4.601 | **4.611** |

[a]HS: Hashin-Shtrikman lower and upper bounds; S: *Salje's* [2007] interface factor (0 = no interfacial effects; 1 = only interfacial effects); GAV = Geometric mean of the four HS values.

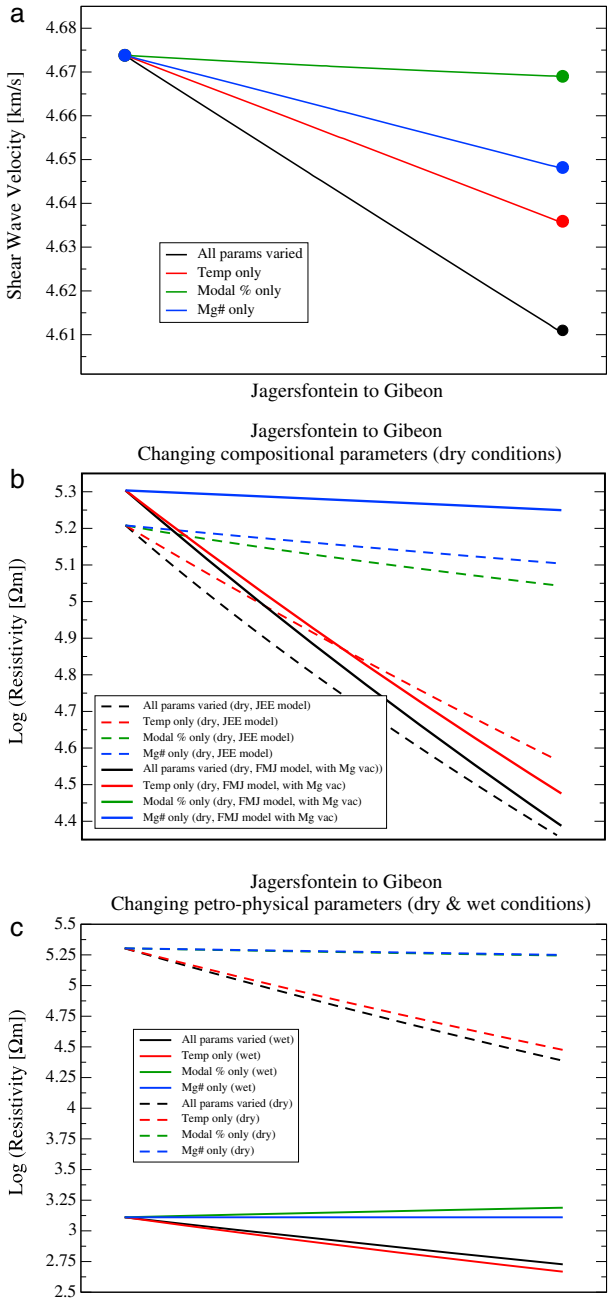


**Figure 2.** (a) Variation of expected shear wave velocity going from Jagersfontein temperature, modal composition, and Mg# parameters to Gibeon parameters. Black line: varying all three simultaneously. Red line: varying only temperature. Blue line: varying only Mg#. Green line: varying only composition. (b) Variation of log(resistivity) going from Jagersfontein temperature, modal composition, and Mg# parameters to Gibeon parameters for the *Jones et al*. [2009a] (JEE) and *Fullea et al*. [2011] (FMJ) models of small polaron conduction, with magnesium vacancies for the FMJ model and dry conditions. Black lines: varying all three simultaneously. Red lines: varying only temperature. Green lines: varying only modal mineralogy (note that the solid green line for FMJ model varying composition only lies beneath the solid blue line for FMJ model varying Mg# only). Blue lines: varying only Mg# (note that the green lines lie beneath the blue ones). (c) Variation of log (resistivity) going from Jagersfontein temperature, modal composition, and Mg# parameters to Gibeon parameters for the *Fullea et al*. [2011] (FMJ) model of small polaron conduction, with magnesium vacancies for the FMJ model (dashed lines) and "wet" conditions (solid lines), where wet means 80 ppm water in Ol, 200 ppm in Opx, 300 ppm in Cpx, and none in Gt. Black lines: varying all three simultaneously. Red lines: varying only temperature. Green lines: varying only modal composition (note that the dashed green line for FMJ small polaron model varying modal composition only lies beneath the dashed blue line for FMJ small polaron model varying Mg# only). Blue lines: varying only Mg# (note that the green lines lie beneath the blue ones).

[2011] (equations (2), solid lines), where the minor (less than 0.025 log units) effects of magnesium vacancies have been considered in the latter. The differences are within 0.1 log units of each other, with the main difference being that the temperature effect is more dominant in the *Fullea et al.* [2011] model than the *Jones et al.* [2009a] one. However, these differences are completely overshadowed by the very large effects of proton conductivity when wet conditions are included (discussed below). For the following calculations, we will adopt the *Fullea et al.* [2011] model for small polaron conduction and magnesium vacancies and the recent *Jones et al.* [2012] values for proton conduction.

[25] The whole rock conductivity calculations for varying from Jagersfontein to Gibeon temperature ($T$), Mg#, and modal% for wet conditions, where wet means 80 wt ppm $H_2O$ in Ol, 200 ppm in Opx, 300 ppm in Cpx, and 0 ppm in Gt and Sp, compared to dry conditions are shown in Figure 2c. The variations of temperature, Mg# and modal% are all assumed to be linear with distance from Jagersfontein to Gibeon. We recognize that the parameters may vary laterally along more complex paths, with perhaps shaper gradients at the craton boundary, but we make here the simplest possible assumption. It is unlikely that the paths for temperature, modal%, and Mg# fall outside the bounds represented by the Jagersfontein and Gibeon values, so the paths will be monotonic, either decreasing or increasing. For electrical conductivity, the only parameter of concern is temperature, and a linear assumption of increasing temperature from Jagersfontein to Gibeon is reasonable. For $V_s$ velocity, temperature represents some 70% of the change, and the rest is due to compositional variation (Mg# and modal%). For composition, a more step-like path is probably more likely going from on-craton to off-craton, but we have insufficient knowledge of that path to be able to characterize it with any confidence. Any effect though will be second order.

[26] The effects of water concentration on the whole rock calculations are shown in Table 7 and in Figure 3 for Jagersfontein (black point and line) and Gibeon (red point and line). Totally dry conditions are shown by the two points along the ordinate, and wet conditions, with $C_w$ ($C_w$ = water content in wt ppm) in Ol varying from 0 to 200 ppm and $C_w$ in Opx, Cpx, and Gt fixed at 200, 300, and 0 ppm, respectively, by the two lines. There is a rapid decrease in resistivity from dry to 50 ppm by 2 orders of magnitude, then a leveling off with further increases in $C_w$ in Ol such that the decrease in resistivity from 150 ppm to 200 ppm is less than a quarter of an order of magnitude (Table 8).

**Table 7.** Estimates of $\log_{10}$(Resistivity [Ωm]) of Olivine at 100 km Depth beneath Jagersfontein (FRB Samples) and Gibeon (KGG Samples), Assuming Wet Conditions, with Olivine Varying from 0 to 200 ppm and Opx, Cpx, and Gt Fixed at 200, 300, and 0 ppm, Respectively

| | FRB AV | KGG AV |
|---|---|---|
| Ol wt ppm $H_2O$ | HS GAV | HS GAV |
| 0 | 4.27 | 3.83 |
| 10 | 3.63 | 3.29 |
| 20 | 3.48 | 3.12 |
| 40 | 3.30 | 2.93 |
| 60 | 3.18 | 2.81 |
| 80 | 3.10 | 2.72 |
| 100 | 3.03 | 2.65 |
| 150 | 2.90 | 2.52 |
| 200 | 2.81 | 2.42 |

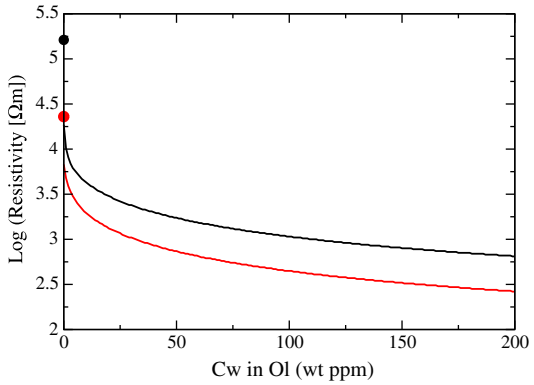


**Figure 3.** Electrical resistivity of whole rocks for Jagersfontein (black line) and Gibeon (red line) for dry conditions (points) and for varying water content in olivine from 0 to 200 ppm, with water contents in Opx, Cpx, and Gt fixed at 200 ppm, 300 ppm, and 0 ppm, respectively.

[27] As noted previously by *Jones et al.* [2009a], who compared the Slave craton to the Kaapvaal craton, the temperature variation in cratonic lithosphere accounts for almost 70% of the seismic variation (Figure 2a) and, if the water content is known, 90% of the resistivity variation (Figures 2b and 2c). Modal compositional variation causes small (velocity) to negligible (resistivity) effects for both parameters. Increasing iron content has the effect of decreasing both $V_s$ and resistivity—the former due to the increase in density being greater than the commensurate increase in the shear modulus and the latter due to more iron in the lattice structure. This variational behavior can be examined in terms of a cross-plot between log($\rho$) and $V_s$, shown in Figure 4a for varying all parameters

**Table 8.** Laboratory-derived Estimates of $V_s$ Velocity and Dry and Wet (80 ppm Ol, 200 ppm Opx, 300 ppm Cpx) $Log_{10}$(resistivity) and Their Maximum and Minimum Ranges at 100 km Depth for Jagersfontein and Gibeon

| Location | Average $V_s$ (km/s) | $\sigma$ | Dry | | Wet | |
|---|---|---|---|---|---|---|
| | | | Average $Log_{10}(\rho)$ | ±Range | Average $Log_{10}(\rho)$ | ±Range |
| Jagersfontein (−29.8°N, +25.4°W) | 4.674 | 0.002 | 5.21 | 0.17 | 3.10 | 0.075 |
| Gibeon (−25.1°N, +17.8°W) | 4.611 | 0.0055 | 4.36 | 0.26 | 2.72 | 0.050 |

linearly from Jagersfontein conditions to Gibeon conditions, assuming dry conditions (dashed line) and wet conditions with the water contents of [80, 200, 300, 0] for [Ol, Opx, Cpx, Gt] for both Jagersfontein and Gibeon. As $V_s$ is, to first order, proportional to $T$, and log(resistivity) proportional to $1/T$, then (1/log(resistivity))-$V_s$ will vary linearly, so we plot $V_s$ against 1/log(resistivity) in Figure 4b for dry conditions and wet conditions, with $C_w$ in Ol varying from 0 to 300 ppm and $C_w$ in Opx, Cpx, and Gt fixed at 200, 300, and 0 ppm, respectively. Regressions to the linear relationships of inverse(log(resistivity)) against $V_s$ velocity in Figure 4b are given in Table 9 and shown in Figure 5, where

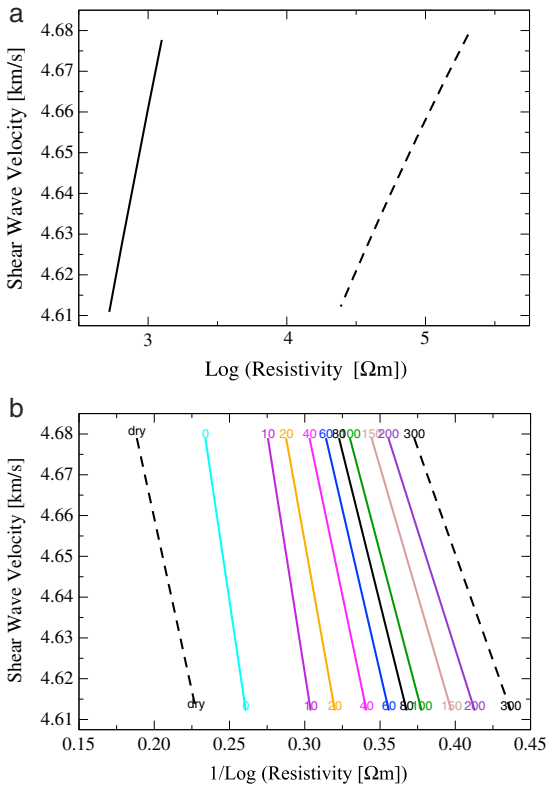


**Figure 4.** (a) Cross-plot of log(resistivity) against shear wave velocity ($V_s$) varying from Jagersfontein parameters (J) to Gibeon ones (G). Solid black line: Varying temperature, modal composition and Mg# simultaneously for a wet model with 80 wt ppm water in Ol, 200 ppm in Opx, 300 ppm in Cpx, and 0 ppm in Gt (proton conduction dominates). Dashed black line: varying temperature, modal composition, and Mg# simultaneously for a dry model (small polaron conduction only). Note that the cross-plot relationship is not linear but curvilinear. (b) Cross-plot of 1/log(resistivity) against shear wave velocity ($V_s$) varying from Jagersfontein parameters to Gibeon ones for varying water content in olivine. From dry conditions (no water in any mineral), to 0 to 300 ppm water in Ol, 200 ppm in Opx, 300 ppm in Cpx, and 0 ppm in Gt.

**Table 9.** Intercept and Gradient of Linear Relationships between 1/(log(Resistivity)) and $V_s$ for Varying $C_w$ in Olivine, as Shown in Figure 4b

| Water Content in Olivine | Intercept | Gradient |
|---|---|---|
| Dry | 4.998 | −1.693 |
| 0 | 5.261 | −2.486 |
| 10 | 5.326 | −2.349 |
| 20 | 5.272 | −2.062 |
| 40 | 5.214 | −1.765 |
| 60 | 5.181 | −1.598 |
| 80 | 5.159 | −1.486 |
| 100 | 5.142 | −1.402 |
| 150 | 5.113 | −1.259 |
| 200 | 5.093 | −1.165 |
| 300 | 5.067 | −1.041 |

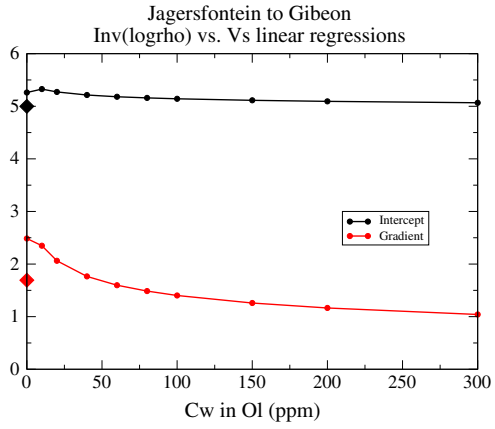


**Figure 5.** Variation of linear regression intercept and gradient with water content in olivine for whole rock inverse(log(resistivity)) versus $V_s$ velocity shown in Figure 4b.

$$V_{s,100}(\rho_{100}, C_w) = \text{Intercept}(C_w) + \text{Gradient}(C_w)/\log(\rho_{100}) \quad (3)$$

and $C_w$ is water content in wt ppm. This functional relationship for varying $\rho$ will be tested on field data in the following.

## 3. Geophysical Observations

### 3.1. Seismological Observations and Model Depth Slices

[28] Seismic shear wave velocities at 100 km beneath Southern Africa were taken from the shear wave velocity model of *Fishwick* [2010], in which tomographic models were calculated for a series of depth slices using over 12,000 surface waveforms. In this study, we use the high-resolution model for southern Africa, where the velocity variations are represented by a spherical spline function with knot points at 1.5° (see Fig. 4 of *Fishwick* [2010]). This particular seismic model is chosen as opposed to others as it has the highest resolution while imaging structure across the whole of the southern part of the continent. Interstation surface wave measurements and surface wave array tomography [e.g., *Larson et al.*, 2006; *Li and Burke*, 2006; *Chevrot and Zhao*, 2007; *Adams and Nyblade*, 2011; *Li*, 2011] or body wave studies [e.g., *Fouch et al.*, 2004] produce higher resolution images for the region directly beneath the Kaapvaal Craton but provide no information on the regional velocity structure. Alternative continental or global models [e.g., *Lebedev and van der Hilst*, 2008; *Priestley et al.*, 2008; *Ritsema et al.*, 2011] provide good representation of the longer wavelength structure but, because of their parameterizations, do not have as high a resolution as the chosen model. It is worth noting that the choice of the *Fishwick* [2010] model limits detailed discussion of localized features such as the Bushveld complex (see section 6) but is necessary to allow comparison with the excellent coverage obtained from the magnetotelluric experiments.

[29] The map at a depth slice of 100 km is shown in Figure 6, where the tectonic subdivision is taken from *Webb* [2009] and the red and blue open circles represent a 100 km radius around the Jagersfontein and Gibeon kimberlite fields, respectively. Estimates of the uncertainty in absolute velocity are difficult to determine in these tomographic studies. There are two main reasons for this: first, the two-stage nature of the surface wave tomography makes tracking uncertainties between the path-average waveform inversion and the regional tomography difficult; and second, within the tomography parameterization, both the regularization and the data used all contribute to the uncertainties. For Southern Africa, testing of the high-resolution model indicates that when using a reasonable range of damping parameters in the tomographic inversion, the resulting absolute velocities vary by less than ±0.05 km/s. For comparison, from an alternative surface wave technique, *Yang et al.* [2008] use Monte Carlo resampling to estimate uncertainties in shear velocity with a standard deviation of 0.04 km/s throughout the upper mantle beneath the Kaapvaal Craton.

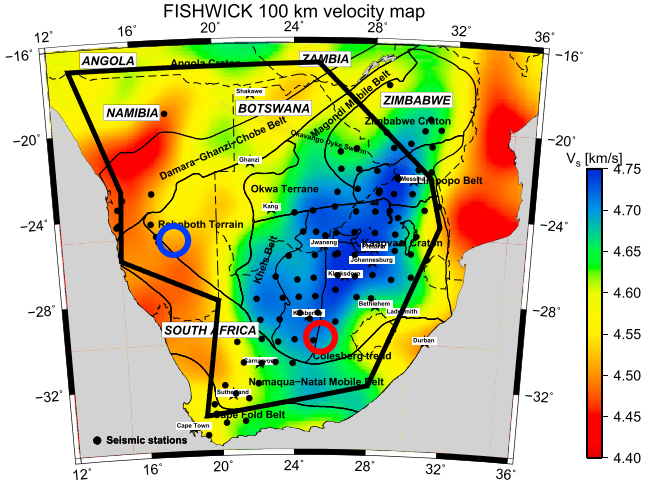


**Figure 6.** Shear wave velocity map at 100 km beneath Southern Africa from *Fishwick* [2010]. The thick black lines enclose the MT mask region for statistical analysis, and the red and blue circles are the locations of the Jagersfontein and Gibeon kimberlite fields, respectively.

[30] A normalized (percentage) histogram of velocity values within the MT mask region (shown in Figure 8) is shown in Figure 7 and of all values on land south of 16°S (red line). The difference between the two histograms arises because the MT mask is focused on the cratonic regions, and we thus remove significant parts of the model that have lower velocities. The average velocity for the whole of southern Africa within the MT mask region is $4.62 \pm 0.08$ km/s, but the distribution is clearly bimodal, with one peak around 4.575 km/s and the second at 4.7125 km/s (Figure 7).

[31] Averaging the model parameters within each circle surrounding the two kimberlite fields gives the mean estimates and $1\sigma$ of the range listed in Table 10 (it must be remembered here that these statistical ranges are of the model parameters, which are derived from smoothing B-spline functions, so will have no outliers extending the tails as often occurs with real data). Xenolith-based estimates of the velocities beneath those localities are 4.67 km/s and 4.61 km/s, respectively, compared to the data-derived tomography modeled velocities of $4.70 \pm 0.01$ km/s and $4.51 \pm 0.01$ km/s (95% confidence intervals on the means). The xenolith-based estimate is marginally lower than the modeled estimate by 0.03 km/s for Jagersfontein, which is within experimental error but is larger by 0.10 km/s for Gibeon, which is about twice the estimated experimental error of 0.05 km/s.

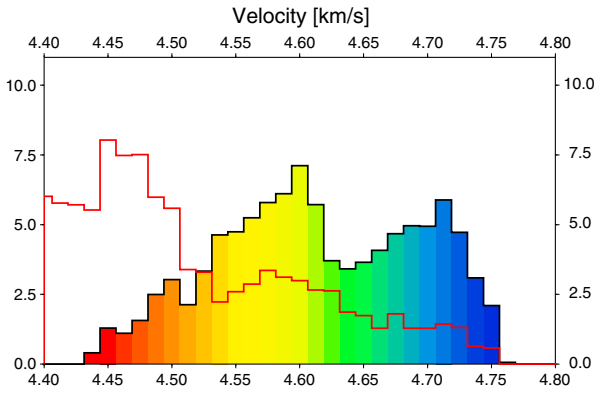


**Figure 7.** Percentage histogram of shear wave velocities at 100 km depth beneath Southern Africa for the MT mask region in Figure 6 (color coding as Figure 6). Histogram of all velocities from the model for locations south of 16°S is shown as the thick red line.

[32] This lack of agreement between the xenolith-derived velocities and the tomographic velocities for Gibeon can be explained in a number of ways. The first consideration is the resolution of the tomographic model. The Gibeon locality is on the western edge of the Rehoboth Terrane, and as such the spatial averaging inherent in the tomographic method may incorporate components of the slower velocities observed on the western margin of the continent, slightly reducing the modeled velocity. *Fishwick et al.* [2008] illustrated how sharp transitions in velocity will be naturally smoothed by the B-spline parameterization over a spatial extent slightly greater than the knot point spacing. Furthermore, in comparison to Jagersfontein, there have been less seismic stations deployed in the region of Gibeon in central Namibia, thus limiting the resolution of the model. Alternatively, we must also consider that the xenoliths date from 70–75 Ma, whereas seismology sees the velocities of today; differences in the predicted and modeled velocities could then be explained by a change in physical properties beneath the region during the last 70 Myr, although the expected reduction in temperature has been accounted for. Finally, as we will show below in our cluster analysis, the median shear wave velocity of cluster 4, which is dominantly MT stations located on the Rehoboth Terrane, is $4.55 \pm 0.035$ km/s, which is within $2\sigma$ of the laboratory-defined value of 4.61 km/s (4.59–4.64 km/s), so indeed it is likely that the effects of the smoothing including lower velocity in the Namaqua-Natal Mobile Belt is the cause of this discrepancy.

## 3.2. Magnetotelluric Observations and Depth Images

[33] Estimates of electrical resistivity at 100 km depth are derived using an approximate depth-transformation coupled with rotational sensitivity and spatial smoothing; the methods used are described in *Jones et al.* [2009b]. An additional smoothing step was performed to obtain images

**Table 10.** Average $V_s$ Velocity and $\text{Log}_{10}$(resistivity) and Their $1\sigma$ Ranges for Estimates from the Velocity and Resistivity Maps at 100 km Depth within 100 km Radius of the Jagersfontein and Gibeon Kimberlite Fields

| Location | Average $V_s$ (km/s) | $\sigma$ | Average $\text{Log}_{10}(\rho)$ | $\sigma$ |
|---|---|---|---|---|
| Jagersfontein (−29.8°N, +25.4°W) | 4.70 | 0.080 | 3.41 | 0.205 |
| Gibeon (−25.1°N, +17.8°W) | 4.51 | 0.075 | 2.78 | 0.090 |

with similar smoothing as that of *Fishwick* [2010], namely a 1.5° Green's function-based smoothing spline was applied using a Singular Value Decomposition (SVD) approach with rejection of small eigenvalues (Generic Mapping Tools [GMT] routine *greenspline* with −C0.00001). Nonphysical log(resistivity) values (<0.0 and >6.5) were rejected, and those otherwise outside the minimum and maximum bounds of [0.5, 6.0] were set to the bounding values prior to smoothing.

[34] The approximate resistivity image at 100 km, given by contouring the maximum resistivity observed at 100 km beneath each site, is shown in Figure 8 on top of the tectonic subdivision of Southern Africa of *Webb* [2009]. A normalized (percentage) histogram of the spline-smoothed values is shown in Figure 9, together with the sample histogram of all observations prior to smoothing (red line). The sample histogram is spatially biased, as more MT sites were located on-craton than off-craton, hence the long large-valued tail. There is a dominant single peak at 3.0 in the histogram, inferring that the mantle at 100 km beneath cratonic southern Africa has a modal value of around 1000 Ωm.

[35] Comparing this approximate resistivity depth image with formal 1-D and 2-D models demonstrates that the image is correct to within reasonable error bounds of one quarter of a decade for most of Southern Africa. The observed averaged log(resistivities) at 100 km beneath Jagersfontein and Gibeon kimberlite fields are 3.41 ± 0.20 and 2.78 ± 0.09 log units. For Jagersfontein, the closest site, *kim015*, has a response that is virtually 1-D (responses in XY and YX directions overlap to within each other's errors), and smooth models give resistivity of 3.30 [see *Jones et al.*, 2012], whereas the 2-D modeling of *Muller et al.* [2009] yields a value of 3.76 ± 0.43. Similarly for Gibeon, the closest MT site, *gib012*, yields a resistivity of 2.65 log units from 1-D modeling and a suggested value of 2.82 ± 0.19 log units from interpolation of the 2-D model of *Muller et al.* [2009].

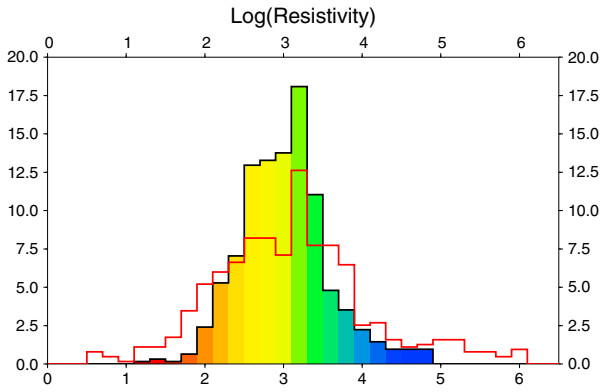


**Figure 9.** Percentage histogram of 1.5° spline-smoothed log(resistivity) values from the image shown in Figure 8 (color coding as Figure 8). The histogram for unsmoothed values is shown as the thick red line.

[36] The resistivity observations derived from the MT data for Jagersfontein and Gibeon are lower than the dry lab-based predictions by almost 2 orders of magnitude (1.6–1.8 log units). Given all

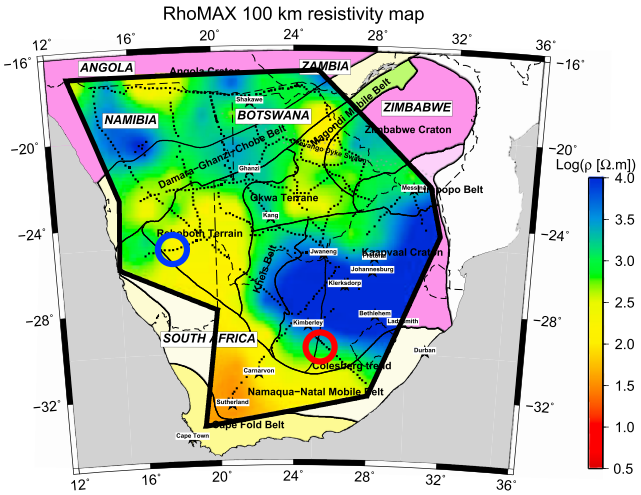


**Figure 8.** RhoMAX Resistivity image at 100 km beneath Southern Africa within the MT mask region constructed as described in *Jones et al.* [2009b] with an additional 1.5° spline smoothing for comparison with the smoothing inherent in the seismic map (Figure 6). The red and blue circles are the locations of the Jagersfontein and Gibeon kimberlite fields, respectively.

plausible explanations for reduced resistivity in the upper mantle of cratonic lithosphere, we deduce that conduction is enhanced due to the presence of water, as concluded in *Fullea et al*. [2011] and *Evans et al*. [2011], based on the xenolith observations of water in mantle minerals discussed above. Given the probable temperature estimates at 100 km depth beneath Jagersfontein and Gibeon, the olivine water model of Karato [*Wang et al*., 2006a] would imply water content below 10 ppm, which is implausibly low. In contrast, the olivine water models of Yoshino [*Yoshino et al*., 2009] and Poe [*Poe et al*., 2010] imply water content estimates that are implausibly high (>350 ppm). *Jones et al*. [2012] proposed a water model for olivine that is consistent with the petrological and geophysical observations beneath Jagersfontein and Gibeon that is listed in Table 2 and is employed herein. That water model implies water content of the order of 40–60 ppm in olivine at 100 km depth for Jagersfontein and Gibeon given the temperature conditions.

## 4. Correlation between Seismic and Electrical images

### 4.1. Least-squares Regression

[37] At a basic qualitative level, one can compare the estimates from the two maps for 100 km depth below Jagersfontein and Gibeon. This correlation is also exhibited at 150 km depth for both compressional and shear wave velocities in *Jones et al*. [2009b]; where velocity is high then electrical resistivity is high, and vice-versa. This correlation encourages us to apply tests whether the relationship is upheld quantitatively and is consistent with that expected from laboratory studies.

[38] A cross-plot of the inverse of the 1/log(resistivity) estimates against their nearest seismic velocity estimate is shown in Figure 10 (black dots), together with a 2-D histogram of the observations (red shading and contours). Also shown in the figure are the laboratory-based inverse(log(resistivity))-$V_s$ linear relationships for dry conditions and 0–300 ppm water in Ol with 200, 300, and 0 ppm water in Opx, Cpx, and Gt, respectively, as shown in Figure 4b. The expected limiting bounds, namely, totally dry (no water in any minerals) and 200 ppm water in Ol, are extended and shown in blue, whereas the 40 ppm water in Ol is shown as the extended dashed black line.

[39] A least-squares best-fitting line to the data, assuming both data are in error [*York*, 1966; *Fasano and Vio*, 1988], using an iterative Huber-based robust scheme replacing values that depart significantly from their $2\sigma$ predictions by their $2\sigma$ predictions [*Huber*, 1981], is

$$V_{s,100} = 5.1045 - 1.4521/\log(\rho_{100}) \quad (4)$$

(solid green line, Figure 10) with a correlation coefficient of −0.71. The 95% confidence intervals on the line are shown by the dashed green lines. The data-defined regression line defined above (equation (4)) matches within 95% error to the lab-based defined regression for 40 ppm water in Ol.

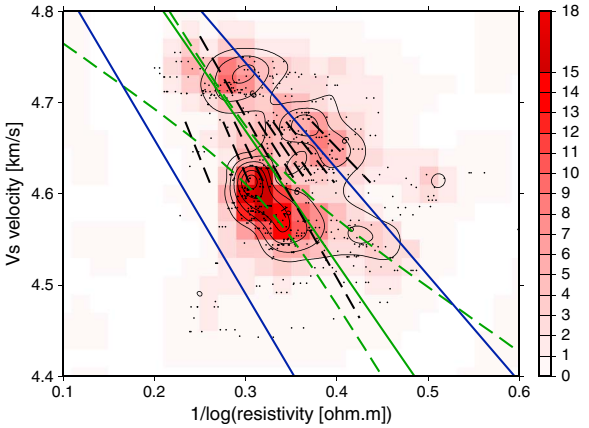


**Figure 10.** Cross-plot of 1/log(resistivity) against shear wave velocity for the two maps shown in Figure 6 (shear wave velocity) and Figure 8 (log(resistivity)). The black dots are the raw, unsmoothed log(resistivity) data, whereas the red shading and contours show the 2-D histogram of the points. The dashed black lines and blue lines are the inferences from the cross-plot of Figure 4b, where the blue lines are the expected extreme conditions, i.e., totally dry conditions and for a water content of [200, 200, 300, 0] ppm in [Ol, Opx, Cpx, Gt], respectively. The solid green line is a robust linear regression to the black points, and the dashed green lines are the 95% confidence intervals of the green line.

[40] Of the 625 estimates available, fully 489 (78%) fall within the range of dry conditions to likely maximum wet conditions (200, 200, 300, 0 ppm in Ol, Opx, Cpx, Gt, respectively). When the uncertainty of ±0.05 km/s on the seismic velocities is considered, then 567 (91%) of the estimates fall within feasible water content bounds.

### 4.2. Cluster Analysis

[41] An alternative statistical approach is to undertake a cluster analysis of the cross-plot of the 1/log (resistivity) estimates against their nearest seismic velocity estimate. Using the fuzzy cluster algorithm

*fanny* of *Kaufman and Rousseeuw* [1990] and examining the normalized Dunn coefficient for 2 to 10 clusters (Figure 11), the Dunn coefficient drops precipitously from five to six clusters. Any more than five clusters results in clusters that are significantly fuzzier compared to fewer clusters.

[42] Those five clusters are shown in Figure 12, together with the laboratory-based inverse(log (resistivity))-$V_s$ linear relationships as for Figure 10. Also shown in the figure and given in Table 11 are the robust centroid locations, given by the median values of each cluster, and the sample standard deviations of each cluster. The mapping of the five clusters spatially onto Southern Africa is shown in the map of Figure 13.

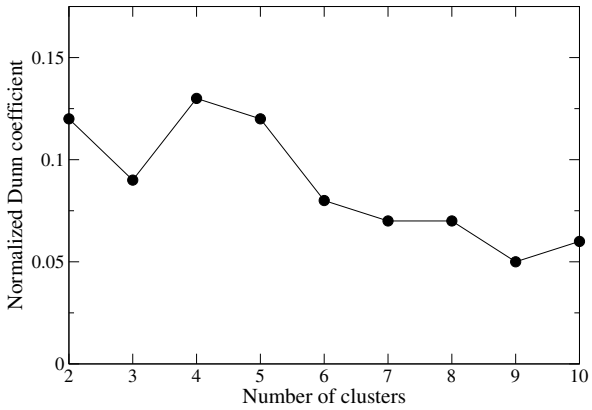


**Figure 11.** Normalized Dunn clustering coefficient for 2 to 10 clusters of the 1/log(resistivity) against $V_s$ cross-plot data shown in Figure 10.

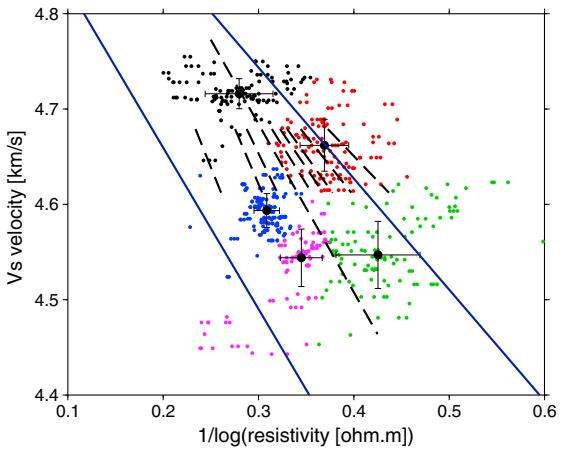


**Figure 12.** Five cluster analysis of the 1/log(resistivity) against $V_s$ cross-plot data. The robust centroids of each cluster are shown by the black dots with one sample standard deviation error bars. The dashed black lines and bordering blue lines are the inferences from the cross-plot of Figure 4b, where the blue lines are the expected extreme conditions, i.e., totally dry conditions and for a water content of [200, 200, 300, 0] ppm in [Ol, Opx, Cpx, Gt], respectively.

[43] Taking the median values for each cluster and assuming linear variation in composition for Southern Africa from Jagersfontein composition and pressure at the lowest temperature to Gibeon composition and pressure at the highest temperature, as listed in Table 3, we can derive an estimate of temperature for each cluster from the averaged $V_s$ velocity values. From the resistivity values, we can estimate the water content.

[44] The clusters form five distinct groupings that can be characterized as follows.

Cluster 1 (black): High velocity/variable resistivity: cold, depleted, variably wet Kaapvaal Craton.

Cluster 1 (black) contains most of the high velocity pairs and spatially the cluster points are located almost entirely on the Kaapvaal Craton. The sample standard deviation for velocity is the smallest of all clusters (±0.016 km/s), but the range of resistivity is the second largest (±0.036 for inverse(log(resistivity))). The high velocity is indicative of cold (620°C), depleted, conditions. The large range in resistivity is indicative of variable water content, from dry to 200 wt ppm, as indicated in the xenolith data of Figure 1.

Cluster 2 (red): High velocity/low resistivity: cold, depleted, very wet, Central Botswana.

Cluster 2 contains high velocity (average 4.66 km/s) and low resistivity (average 500 Ωm) points. Spatially, the points lie almost entirely in central Botswana on the Okwa Terrane and westernmost Zimbabwe Craton beneath the Central Kalahari Game Reserve. At 100 km, the area is relatively cold (average of 765°C), depleted, and wet (average of 200 ppm water in olivine).

Cluster 3 (blue): Moderate velocity/low resistivity: warmer, somewhat less depleted, very dry Angola Craton.

Cluster 3 has the tightest cluster coefficient reflected by the second lowest velocity sample standard error and lowest by far resistivity sample standard error. The velocities are indicative of warm mantle (935°C), but the resistivities imply that the olivine in the mantle is very dry (10 wt ppm). Spatially, the points lie predominantly on the putative southern extension of the Angola Craton, part of the composite Congo Craton, and beneath the Damara-Ghanzi-Chobe Belt and westernmost Okwa Terrane.

**Table 11.** Centroids of the Five Clusters on Figure 12 and Their Errors, and the Inferred Temperatures from Velocity[a] and Water Contents from Resistivity and Temperatures

| Cluster | Inv(Log(Resistivity)) | $V_s$ (km/s) | Resistivity | Temperature (°C) | Water Content |
|---|---|---|---|---|---|
| 1 (black) | $0.280 \pm 0.036$ | $4.72 \pm 0.016$ | 3750 | 620 | 40 |
| 2 (red) | $0.369 \pm 0.026$ | $4.66 \pm 0.027$ | 500 | 765 | 200 |
| 3 (blue) | $0.309 \pm 0.013$ | $4.59 \pm 0.018$ | 1700 | 935 | 10 |
| 4 (green) | $0.425 \pm 0.044$ | $4.55 \pm 0.035$ | 225 | 1035 | 100 |
| 5 (magenta) | $0.345 \pm 0.022$ | $4.54 \pm 0.030$ | 800 | 1050 | 20 |

[a]Assuming linearly varying composition across southern Africa from Jagersfontein conditions at lowest temperature to Gibeon conditions at highest temperature as listed in Table 4.

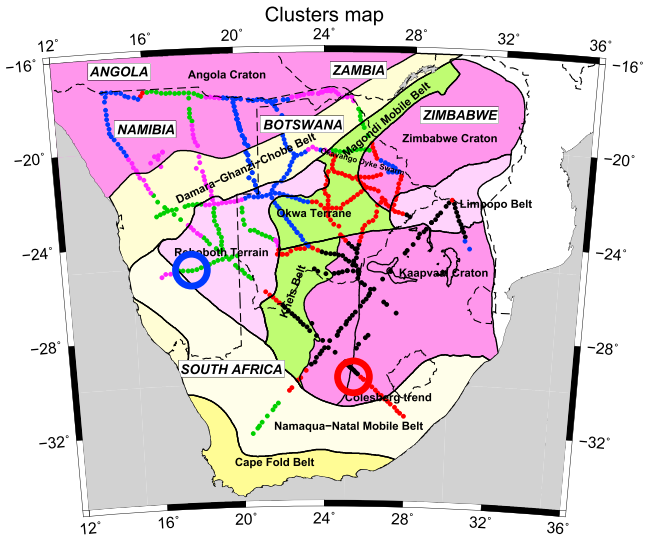


**Figure 13.** Mapping of the five clusters onto the MT site locations of Southern Africa.

Cluster 4 (green): Low velocity/very low resistivity: warm, fertile, very wet, Rehoboth Terrane.

This cluster has the lowest clustering coefficient, as indicated by having the largest sample standard deviations ($\pm 0.044$ and $\pm 0.035$ for Inv(log(rho)) and $V_s$, respectively). The influence of the obvious outliers lying well above the 200 ppm water conditions line was downweighted by deriving the median of the cluster rather than the mean. Spatially, the cluster points are dispersed, but most of the locations on the Rehoboth Terrane fall into this cluster. Velocity is low (4.55 km/s), indicative of warm and fertile conditions at 100 km, and resistivity is low (225 Ωm), indicative of wet conditions (100 ppm water in olivine). Such conditions were concluded for the Rehoboth Terrane in the modeling and interpretation of *Muller et al.* [2009] of the MT data along the SE-NW profile from Jagersfontein to the Damara belt.

Cluster 5 (magenta): Low velocity/moderate resistivity: warm, fertile, dryer Damara Belt.

Cluster 5 is relatively tight in its center. As above, the influence of the obvious outliers lying below the dry conditions line was downweighted by deriving the median of the cluster rather than the mean. The velocities are as low as those of cluster 4, and spatially the two clusters overlap and lie primarily within Namibia on the Damara Belt and the Rehoboth Terrane. The seismic low-velocity "tongue" into the Angola Craton in north-central Namibia is reflected by the points from these two clusters.

[45] If four clusters are derived from the cross-plot points, then clusters 4 and 5 above coalesce into a single cluster.

## 5. Predictions of Velocity and Water Content

[46] Using the linear relationship between inverse log(resistivity) and $V_s$ velocity defined by equation (4), we can predict the velocity at 100 km from the imaged resistivity map (Figure 8) to produce Figure 14. A difference map, formed from the modeled

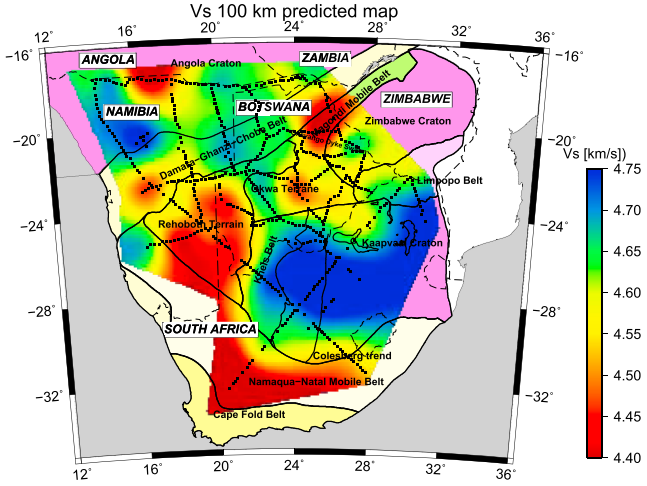


**Figure 14.** Predicted velocity map of Southern Africa using the log(resistivity) map of Figure 8 using the relationship given by the thick green line in Figure 10 of $V_{s,100} = 5.1045 - 1.4521/\log(\rho_{100})$.

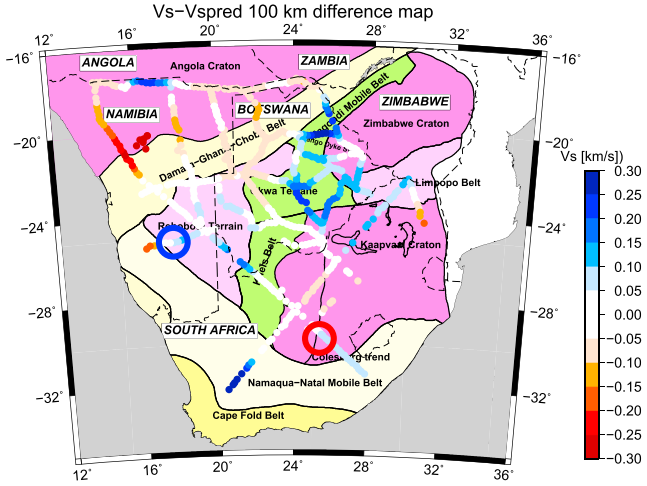


**Figure 15.** Difference between the seismic modeled velocity of Figure 6 and the prediction of the velocity from the log(resistivity) map of Figure 8 using the relationship given by the thick green line in Figure 10 of $V_{s,100} = 5.1045 - 1.4521/\log(\rho_{100})$. Transparent regions are where the differences are less than $\pm 0.05$ km/s.

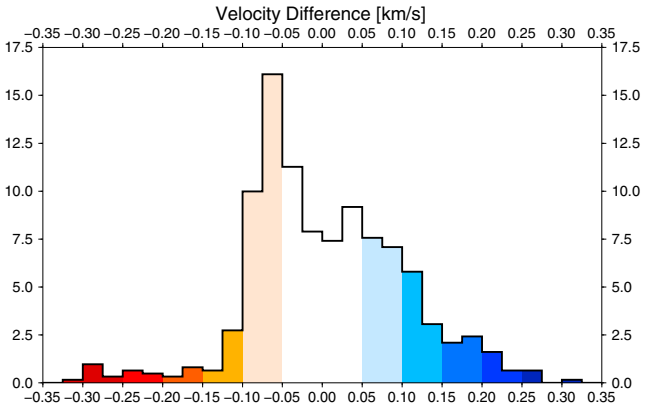


**Figure 16.** Percentage histogram of velocity differences shown in Figure 15 (using the same color coding as Figure 15).

velocity map (Figure 6) minus the electrically predicted velocity map (Figure 14), is shown in Figure 15 and a histogram of the differences in Figure 16. The largest positive differences (blue), i.e., electrical resistivity values underestimate velocity, occur in the region affected by Bushveld magmatism. As noted previously by *Evans et al.* [2011], the mantle lithosphere of the eastern Kaapvaal Craton is characterized by a region of very low resistivities that spatially correlate with the Bushveld Complex. South African Seismic Experiment (SASE) body wave studies showed the region to also exhibit anomalously low velocities [*Fouch et al.*, 2004]. Recent surface wave tomographic images by *Li* [2011], based on the seismic data from the SASE data only, exhibit greater lateral variability than that shown in Figure 6, which is a map of regional structure. In particular, the images at 80–100 km and 100–120 km show strong reduction (up to −5% velocity perturbation) exactly in the region mapped by the blue points. But such velocity reductions are not consistent with the very large resistivity reductions. The cause of the high conductivity is unknown, and graphite, iron-rich garnet, and/or metallic sulfides are all suggested, and of these the amount of iron-rich garnet is the candidate that will significantly reduce seismic velocity. The region of NW Namibia just on the magnetically defined southern boundary of the Angola Craton, where electrical resistivity predicts *higher* velocity than observed (red points), is far more difficult to explain. This again may be due to the smoothing inherent in the tomographic imaging that includes lower velocities associated with the offshore region.

[47] Using the observed values of $V_s$ (Figure 6) and log(resistivity) (Figure 8), we can derive the water content in olivine by determining the relative position on the inverse(log(resistivity)) versus $V_s$ cross-plot (Figure 10) against the laboratory determined predictions (dashed lines on Figure 10), under the assumption that the water content in Opx and Cpx is uniform at 100 km across Southern Africa at 200 ppm and 300 ppm, respectively. We only perform this prediction up to water contents of 300 wt ppm in olivine; higher values are discarded as being indicative of another conductive process operating. Noticeable in the water prediction map of Figure 17 is that the area of Jagersfontein appears to be anomalously wetter compared to the rest of the Kaapvaal Craton and indeed compared to much of cratonic Southern Africa.

[48] With the exception of the Bushveld Complex region and the area on the northern border of Namibia, the high water content areas are all associated with the tectonic/mobile belts: Limpopo, Magondi, and Namaqua-Natal belts. The portion of the Okwa Terrane characterized by higher water contents has been inferred to be part of the Magondi Belt wrapping around the Zimbabwe Craton—based on interpretation of the southern African magnetic anomaly map. The high water contents have implications for the rheological strength of the cratons versus mobile/tectonic belts.

[49] The histogram of water contents is shown in Figure 18 for the MT locations, and clearly there is a very strong indication of low water content <50 ppm over most of cratonic Southern Africa.

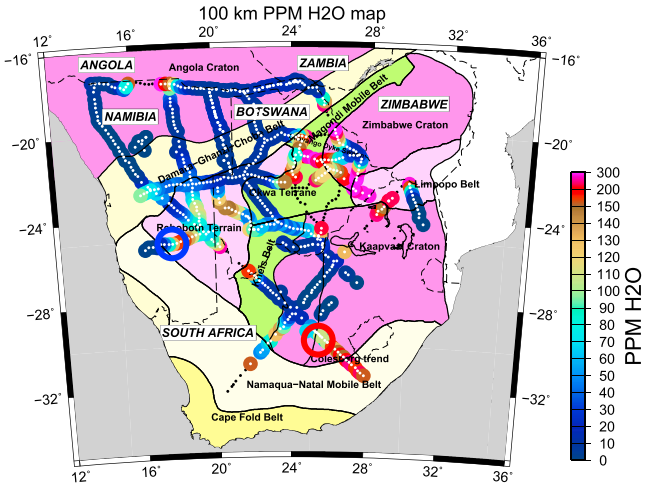


**Figure 17.** Predicted water content in olivine based on the observed values of $V_s$ (Figure 6) and log(resistivity) (Figure 8) from the relative position on the inverse(log(resistivity)) versus $V_s$ cross-plot (Figure 10) against the laboratory determined predictions (dashed lines on Figure 10), under the assumption that the water content in Opx and Cpx is uniform at 100 km across Southern Africa at 200 ppm and 300 ppm, respectively.

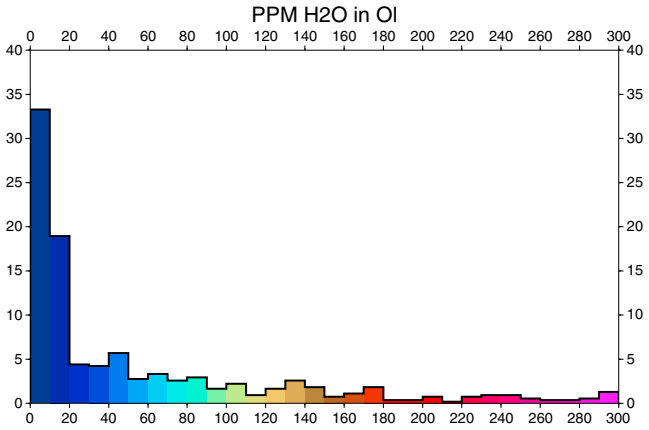


**Figure 18.** Percentage histogram of water content estimates shown in Figure 17 for the 625 locations in Southern Africa.

## 6. Discussion

[50] Laboratory-defined considerations lead to derivable relationships for cratonic lithospheric mantle between seismic velocity and electrical resistivity through primarily, but not exclusively, the sensitivity of both to lateral variation in temperature. In contrast, resistivity is highly sensitive to water content, whereas seismic velocity is insensitive at the levels expected in cratonic mantle lithosphere (<200 wt ppm in olivine). As discussed by, e.g., *Karato* [2006], a 1% reduction in velocity will occur for a 1 wt % (10,000 wt ppm) increase in water, meaning that water contents of order <0.1% (1000 ppm) produce negligible effects on velocity. A far greater, and observable, effect is caused on seismic attenuation by relatively low orders of water [e.g., *Karato*, 2006]; however, herein we are considering solely seismic velocity.

[51] Using seismic velocity to control temperature variation, the variation in electrical resistivity can be used to infer water content, provided one can make valid assumptions about water partitioning between the minerals. In our case, we assume that the water content in olivine is the only one that varies laterally, and that the water contents in the pyroxenes are uniform at 200 wt ppm and 300 wt ppm for Opx and Cpx, respectively, with no water in garnet. This assumption, rather than assuming a particular water partitioning, such as 1:2:3 for Ol : Opx : Cpx as adopted in *Jones et al.* [2012], has little effect on the water content mapping as the lithospheric mantle is dominated by Ol with very little Cpx. Any errors will mean that the absolute values are modified, but the relative differences will remain.

[52] A map of water content in olivine at 100 km, based on the lab-based considerations applied to a cross-plot between the resistivity and velocity observations, shows low values (<50 wt ppm) for the bulk of cratonic Southern Africa, with the area of Jagersfontein being anomalously higher than much of the Kaapvaal Craton (average of 40 wt ppm) but consistent with the xenolith-determined values of the order of 80 ppm, as observed in xenolith samples. The Rehoboth Terrane appears wetter than the Kaapvaal Craton, with an average of 100 wt ppm in olivine. Intriguingly, the southern extension of the Angola Craton appears to be the driest lithosphere in Southern Africa, implying strongest rheology. In contrast, the western boundary of the Zimbabwe Craton appears to be very wet, of the order of 200 wt ppm, as do the stitching mobile belts, attesting to their weaker rheology and deformation between the three cratons (Kaapvaal, Zimbabwe, and Angolan cratons).

[53] From the observations we derive a data-defined, robust linear regression between the (inverse of) electrical resistivity values and closest shear wave velocity modeled estimates, assuming both are in error. Satisfyingly, the regression is statistically the same as that derived independently from petrological-geophysical arguments for a water content of 40 wt ppm in olivine. That this is so attests to the dominance of bulk properties in defining electrical resistivity for most of Southern Africa rather than the effects of an interconnected minor phase. Applying the determined data-derived regression equation, we predict shear wave velocity at 100 km from the electrical resistivity map and obtain the differences between the modeled and predicted velocities. For most of southern Africa, the differences lie within experimental error of ±0.05 km/s. This means that for most of southern Africa lateral variations in electrical resistivity and shear wave velocity are related, implying that temperature control and water content are

the dominant factors and that lateral compositional variation is a minor second-order effect. The discrepancies lie in two regions, one dominated by Bushveld magmatism that introduced a phase that reduces velocity by up to −5% but that significantly reduces electrical resistivity to an even greater extent. The other is located in NW Namibia on the southern edge of the Angola Craton, where electrical resistivity would suggest higher values of velocity than those modeled tomographically. While there are only limited seismic stations in the region of the Angolan Craton, using a model constructed from regional surface wave tomography means that good path coverage can be obtained even in the absence of stations. Due to the location of sources and receivers across the continent, and the large number of data included in the study, this area has good path coverage [see *Fishwick*, 2010]. Clearly, stations in the region will improve future generations of models, but the fundamental features are unlikely to change significantly.

[54] Critical to the analysis is the assumption made of the appropriate water model for olivine, namely that of *Jones et al*. [2012] rather than the models of Karato [*Wang et al*., 2006b], Yoshino [*Yoshino et al*., 2009], or Poe [*Poe et al*., 2010]. None of those three other models would have resulted in the striking consistency between the data-defined regression and the laboratory-defined one, which lends further support to the *Jones et al*. [2012] model.

## 7. Conclusions

[55] Combining high quality seismic and electromagnetic data can yield regional-scale geophysical-petrological information that cannot be obtained by any other means. Consideration of the moduli, density, and electrical conductivity based on laboratory-determined empirical equations for individual mantle minerals suggests that, in the absence of minor highly conducting phases, there should be a simple linear relationship between velocity and inverse log(resistivity) that is a function of temperature and water content for the lithospheric mantle. This hypothesis is tested on data from Southern Africa, where we show that the linear relationship is upheld for 80% of Southern Africa. Furthermore, we demonstrate that the relationship is statistically close to that which is expected when going from Jagersfontein parameters to Gibeon parameters for an average water content of 40 wt ppm in olivine.

[56] There are many kimberlite sites across the whole of the Kaapvaal Craton that could have been used to calibrate our approach. However, we needed three things for this study to establish the methodology: (1) good control on mineralogy and temperature, (2) very good estimates of electrical conductivity at the chosen depth preferably where 1-D is valid, and (3) estimates of the water content at depth. Of these three, (3) is the most restrictive, in that we have water content estimates in olivine at very, very few locations, and (2) is the next most restrictive. As it happens, only one location meets all three of these criteria, and that is the Jagersfontein kimberlite area. For the Gibeon area, we have only two of these (1 and 2) and have to guess the water content. Also, our paper is meant to present a methodology, with an example of application of the methodology. It is not meant to be a systematic study. This approach can be applied for Southern Africa given the simple mineralogy within the lithosphere. Whether it can be more broadly applied needs to be established.

[57] We have made several assumptions during this exposition, such as laterally uniform water content in the pyroxenes and characterizing the end-member compositions by those observed in xenoliths beneath Jagersfontein and Gibeon. Any error in any of them will affect the absolute values of the laboratory-defined inverse(log(resistivity)) to $V_s$ relationship, but that the data-defined relationship correlates almost perfectly with the laboratory-defined one for 40 wt ppm in olivine lends significant support to our assumptions being valid.

[58] Finally, there is no doubt whatsoever that we must take a holistic view in any modeling and interpretation of geophysical data. We should not model one type of data at the expense of all others. Herein we demonstrate the advantages of considering seismic and electrical data within an integrated geophysical-petrological framework. Knowing that this is possible leads us to use more sophisticated holistic tools, such as the LitMod approach of Afonso, Fullea, and colleagues [*Afonso et al*., 2008; *Fullea et al*., 2009; *Fullea et al*., 2011].

## Acknowledgments

[59] The geosciences are data driven. Large-scale geophysical projects such as SASE (Southern African Seismic Experiment, *James et al*. [2001]) and SAMTEX (Southern African Magnetotelluric Experiment, *Jones et al*. [2009b]) are invaluable for providing data that yields insights into Earth structure and processes, but these cannot take place without a huge group of committed individuals, institutions, and agencies. Those

involved in SAMTEX are listed in the Acknowledgements in *Jones et al*. [2009b], and we wish to again acknowledge the three main funding agencies, the U.S. National Science Foundation's Continental Dynamics Program (grant EAR0455242 to RLE), the South African Department of Science and Technology (grant to South African Council for Geoscience), and Science Foundation Ireland (grant 05/RGP/GEO001 to AGJ), for their support. Industry support for SAMTEX from De Beers Group Services, BHP Billiton and Rio Tinto Mining and Exploration resulted in a program far more extensive than originally conceived. S.F. has been supported by the NERC New Investigator grant NE/G000859/1. M.M. wishes to thank Science Foundation Ireland (grant 08/RFP/GEO1693 SAMTEX to AGJ) for support. J.F. wishes to thank Enterprise Ireland (grant Topo-Med to AGJ), Science Foundation Ireland (grant 10/IN.1/I3022 IRETHERM to AGJ), and the JAE-DOC Programme from Spanish CSIC, cofunded by FSE for support. Finally, we wish to thank the Editor, Thorsten Becker, and our two reviewers, one of whom was David James, for their thoughtful and careful reviews of the submitted version of our paper.

## References

Adams, A., and A. Nyblade (2011), Shear wave velocity structure of the southern African upper mantle with implications for the uplift of southern Africa, *Geophys. J. Int.*, *186*(2), 808–824.

Afonso, J. C., M. Fernandez, G. Ranalli, W. L. Griffin, and J. A. D. Connolly (2008), Integrated geophysical-petrological modeling of the lithosphere and sublithospheric upper mantle: Methodology and applications, *Geochem. Geophys. Geosyst.*, *9*, doi: 10.1029/2007gc001834.

Bai, Q., and D. L. Kohlstedt (1992), Substantial hydrogen solubility in olivine and implications for water storage in the mantle, *Nature*, *357*(6380), 672–674.

Baptiste, V., A. Tommasi, and S. Demouchy (2012), Deformation and hydration of the lithospheric mantle beneath the Kaapvaal craton, South Africa, *Lithos*, *149*, 31–50.

Bell, D. R., and G. R. Rossman (1992), The distribution of hydroxyl in garnets from the subcontinental mantle of Southern Africa, *Contrib. Mineral. Petrol.*, *111*(2), 161–178.

Berryman, J. G. (1995), Mixture theories for rock properties, in *Rock Physics and Phase Relations: A Handbook of Physical Constants*, edited by T. J. Ahrens, American Geophysical Union, Washington, D.C., USA.

Chevrot, S., and L. Zhao (2007), Multiscale finite-frequency Rayleigh wave tomography of the Kaapvaal craton, *Geophys. J. Int.*, *169*(1), 201–215.

Davis, W. J., A. G. Jones, W. Bleeker, and H. Grutter (2003), Lithosphere development in the Slave craton: A linked crustal and mantle perspective, *Lithos*, *71*(2–4), 575–589.

Duba, A. G., and T. J. Shankland (1982), Free carbon and electrical conductivity in the Earth's mantle, *Geophys. Res. Lett.*, *9*(11), 1271–1274.

Evans, R. L., et al. (2011), The electrical lithosphere beneath the Kaapvaal Craton, Southern Africa, *J. Geophys. Res. Solid Earth*, *116*(B04105), 16, doi: 10.1029/2010JB007883.

Fasano, G., and R. Vio (1988), Fitting a straight line with errors on both coordinates, Bull. Inform. CDS no. 35, Nsl. WG Modern Astron. Meth.

Fishwick, S. (2010), Surface wave tomography Imaging of the lithosphere-asthenosphere boundary beneath central and southern Africa?, *Lithos*, *120*(1–2), 63–73.

Fishwick, S., M. Heintz, B. L. N. Kennett, A. M. Reading, and K. Yoshizawa (2008), Steps in lithospheric thickness within eastern Australia, evidence from surface wave tomography, *Tectonics*, *27*(4).

Fouch, M. J., D. E. James, J. C. VanDecar, S. van der Lee, and G. Kaapvaal Seismic (2004), Mantle seismic structure beneath the Kaapvaal and Zimbabwe Cratons, *S. Afr. J. Geol.*, *107*(1–2), 33–44.

Fullea, J., M. R. Muller, and A. G. Jones (2011), Electrical conductivity of continental lithospheric mantle from integrated geophysical and petrological modeling: Application to the Kaapvaal Craton and Rehoboth Terrane, southern Africa, *J. Geophys. Res. Solid Earth*, *116*, doi: 10.1029/2011JB008544.

Fullea, J., J. C. Afonso, J. A. D. Connolly, M. Fernandez, D. Garcia-Castellanos, and H. Zeyen (2009), LitMod3D: An interactive 3-D software to model the thermal, compositional, density, seismological, and rheological structure of the lithosphere and sublithospheric upper mantle, *Geochem. Geophys. Geosyst.*, *10*, doi: 10.1029/2009gc002391.

Goes, S., R. Govers, and P. Vacher (2000), Shallow mantle temperatures under Europe from *P* and *S* wave tomography, *J. Geophys. Res. Solid Earth*, *105*(B5), 11153–11169.

Grant, K., J. Ingrin, J. P. Lorand, and P. Dumas (2007), Water partitioning between mantle minerals from peridotite xenoliths, *Contrib. Mineral. Petrol.*, *154*(1), 15–34.

Hill, R. (1952), Elastic properties of reinforced solids: Some theoretical principles, *Proc. Phys. Soc. London, Ser. A*, *65*, 349–354.

Hirschmann, M., and D. Kohlstedt (2012), Water in Earth's mantle, *Phys. Today*, *65*(3), 40–45.

Huber, P. J. (1981), *Robust Statistics*, 308 pp., John Wiley, New York.

Ingrin, J., and H. Skogby (2000), Hydrogen in nominally anhydrous upper-mantle minerals: Concentration levels and implications, *Eur. J. Mineral.*, *12*(3), 543–570.

James, D. E., M. J. Fouch, J. C. VanDecar, S. van der Lee, and Kaapvaal Seismic Group (2001), Tectospheric structure beneath southern Africa, *Geophys. Res. Lett.*, *28*(13), 2485–2488.

James, D. E., F. R. Boyd, D. Schutt, D. R. Bell, and R. W. Carlson (2004), Xenolith constraints on seismic velocities in the upper mantle beneath southern Africa, *Geochem. Geophys. Geosyst.*, *5*, 32, doi: 10.1029/2003GC000551.

Ji, S., Q. Wang, B. Xia, and D. Marcotte (2004), Mechanical properties of multiphase materials and rocks: A phenomenological approach using generalized means, *J. Struct. Geol.*, *26*, 1377–1390.

Jones, A. G. (1992), Electrical conductivity of the continental lower crust., in *Continental Lower Crust*, edited by D. M. Fountain, R. J. Arculus and R. W. Kay, pp. 81–143, Amsterdam, Elsevier.

Jones, A. G. (1998), Waves of the future: Superior inferences from collocated seismic and electromagnetic experiments, *Tectonophysics*, *286*(1–4), 273–298.

Jones, A. G. (1999), Imaging the continental upper mantle using electromagnetic methods, *Lithos*, *48*(1–4), 57–80.

Jones, A. G., R. L. Evans, and D. W. Eaton (2009a), Velocity-conductivity relationships for mantle mineral assemblages in Archean cratonic lithosphere based on a review of laboratory data and Hashin-Shtrikman extremal bounds, *Lithos*, *109*(1–2), 131–143, doi: 10.1016/j.lithos.2008.10.014.

Jones, A. G., J. Fullea, R. L. Evans, and M. R. Muller (2012), Calibrating laboratory-determined models of electrical conductivity of mantle minerals using geophysical and

petrological observations, *Geochem. Geophys. Geosyst.*, *13*, doi: 10.1029/2012GC004055.

Jones, A. G., et al. (2009b), Area selection for diamonds using magnetotellurics: Examples from southern Africa, *Lithos*, *112*, 83–92, doi: 10.1016/j.lithos.2009.06.011.

Jones, M. Q. W. (1988), Heat flow in the Witwatersrand Basin and environs and its significance for the South African shield geotherm and lithosphere thickness, *J. Geophys. Res. Solid Earth Planets*, *93*(B4), 3243–3260.

Karato, S. (2006), Remote sensing of hydrogen in Earth's mantle, in *Water in Nominally Anhydrous Minerals*, edited by H. Keppler, and J. R. Smyth, *Rev. Min. Geochem.*, *62*, 343–375.

Kaufman, L., and P. J. Rousseeuw (1990), *Finding Groups in Data: An Introduction to Cluster Analysis*, Wiley, New York.

Kobussen, A. F., W. L. Griffin, and S. Y. O'Reilly (2009), Cretaceous thermo-chemical modification of the Kaapvaal cratonic lithosphere, South Africa, *Lithos*, *112*, 886–895.

Kurosawa, M., H. Yurimoto, and S. Sueno (1997), Patterns in the hydrogen and trace element compositions of mantle olivines, *Phys. Chem. Miner.*, *24*(6), 385–395.

Kuskov, O. L., and V. A. Kronrod (2006), Determining the temperature of the Earth's continental upper mantle from geochemical and seismic data, *Geochem. Int.*, *44*(3), 232–248.

Larson, A. M., J. A. Snoke, and D. E. James (2006), *S*-wave velocity structure, mantle xenoliths and the upper mantle beneath the Kaapvaal craton, *Geophys. J. Int.*, *167*(1), 171–186.

Lebedev, S., and R. D. van der Hilst (2008), Global upper-mantle tomography with the automated multimode inversion of surface and *S*-wave forms, *Geophys. J. Int.*, *173*(2), 505–518.

Li, A. (2011), Shear wave model of southern Africa from regional Rayleigh wave tomography with 2-D sensitivity kernels, *Geophys. J. Int.*, *185*, 832–844.

Li, A., and K. Burke (2006), Upper mantle structure of southern Africa from Rayleigh wave tomography, *J. Geophys. Res.*, *111*, doi: 10.1029/2006JB004321.

Liu, W., and B. S. Li (2006), Thermal equation of state of (Mg0.9Fe0.1)(2)SiO4 olivine, *Phys. Earth Planet. Inter.*, *157*(3–4), 188–195.

Muller, M. R., et al. (2009), Lithospheric structure, evolution and diamond prospectivity of the Rehoboth Terrane and western Kaapvaal Craton, southern Africa: Constraints from broadband magnetotellurics, *Lithos*, *112*, 93–105.

Peslier, A. H. (2010), A review of water contents of nominally anhydrous natural minerals in the mantles of Earth, Mars and the Moon, *J. Volcanol. Geotherm. Res.*, *197*(1–4), 239–258.

Peslier, A. H., A. B. Woodland, D. R. Bell, and M. Lazarov (2010), Olivine water contents in the continental lithosphere and the longevity of cratons, *Nature*, *467*(7311), 78–81.

Poe, B. T., C. Romano, F. Nestola, and J. R. Smyth (2010), Electrical conductivity anisotropy of dry and hydrous olivine at 8 GPa, *Phys. Earth Planet. Inter.*, *181*(3–4), 103–111.

Priestley, K., D. McKenzie, E. Debayle, and S. Pilidou (2008), The African upper mantle and its relationship to tectonics and surface geology, *Geophys. J. Int.*, *175*(3), 1108–1126.

Reuss, A. (1929), Berechung der Fliessgrenze von Mischkristallen auf Grund der Plastizitätsbedingung für Einkristalle, *Z. Ang. Math. Mech.*, *9*, 49–58.

Ritsema, J., A. Deuss, H. J. van Heijst, and J. H. Woodhouse (2011), S40RTS: A degree-40 shear-velocity model for the mantle from new Rayleigh wave dispersion, teleseismic traveltime and normal-mode splitting function measurements, *Geophys. J. Int.*, *184*(3), 1223–1236.

Roberts, J. J., and J. A. Tyburczy (1999), Partial-melt electrical conductivity: Influence of melt composition, *J. Geophys. Res. Solid Earth*, *104*(B4), 7055–7065.

Salje, E. K. H. (2007), An empirical scaling model for averaging elastic properties including interfacial effects, *Am. Miner.*, *92*(2–3), 429–432.

Voigt, W. (1928), Lehrbuch der Kristallphysik, Teubner, Leipzig.

Wang, D. J., M. Mookherjee, Y. S. Xu, and S. Karato (2006a), The effect of water on the electrical conductivity of olivine, *Nature*, *443*(7114), 977–980.

Wang, D. J., M. Mookherjee, Y. S. Xu, and S. I. Karato (2006b), The effect of water on the electrical conductivity of olivine, *Nature*, *443*(7114), 977–980.

Watt, J. P., G. F. Davies, and R. J. O'Connell (1976), The elastic properties of composite materials, *Rev. Geophys. Space Phys.*, *14*, 541–563.

Webb, S. (2009), The use of potential field and seismological data to analyze the structure of the lithosphere beneath southern Africa, Unpublished PhD thesis, 377 pp, University of the Witwatersrand, Johannesburg.

Xia, Q. K., Y. T. Hao, P. Li, E. Deloule, M. Coltorti, L. Dallai, X. Z. Yang, and M. Feng (2010), Low water content of the Cenozoic lithospheric mantle beneath the eastern part of the North China Craton, *J. Geophys. Res. Solid Earth*, 115.

Yang, Y., A. Li, and M. H. Ritzwoller (2008), Crustal and uppermost mantle structure in southern Africa revealed from ambient noise and teleseismic tomography, *Geophys. J. Int.*, *174*, 235–248.

York, D. (1966), Least-squares fitting of a straight line, *Can. J. Phys.*, *44*(5), 1079–1086.

Yoshino, T. (2010), Laboratory electrical conductivity measurement of mantle minerals, *Surv. Geophys.*, *31*(2), 163–206.

Yoshino, T., T. Matsuzaki, A. Shatskiy, and T. Katsura (2009), The effect of water on the electrical conductivity of olivine aggregates and its implications for the electrical structure of the upper mantle, *Earth Planet. Sci. Lett.*, *288*(1–2), 291–300.